Mechanical, Morphological, and Charge Transport Properties of NDI Polymers with Variable Built-in Π-Conjugation Lengths Probed by Simulation and Experiment

Dan Zhao, Donghyun Kim, Sarbani Ghosh, Gang Wang, Wei Huang, Zonglong Zhu, Tobin J. Marks, Igor Zozoulenko,* and Antonio Facchetti**

Mechanically deformable polymeric semiconductors are a key material for fabricating flexible organic thin-film transistors (FOTFTs)—the building block of electronic circuits and wearable electronic devices. However, for many π-conjugated polymers achieving mechanical deformability and efficient charge transport remains challenging. Here the effects of polymer backbone bending stiffness and film microstructure on mechanical flexibility and charge transport are investigated via experimental and computational methods for a series of electron-transporting naphthalene diimide (NDI) polymers having differing extents of π-conjugation. The results show that replacing increasing amounts of the π-conjugated comonomer dithienylvinylene (TVT) with the π-nonconjugated comonomer dithienylethane (TET) in the backbone of the fully π-conjugated polymeric semiconductor, PNDI-TVT$_{100}$ (yielding polymeric series PNDI-TVT$_x$, $100 \geq x \geq 0$), lowers backbone rigidity, degree of texturing, and π–π stacking interactions between NDI moieties. Importantly, this comonomer substitution increases the mechanical robustness of PNDI-TVT$_x$ while retaining efficient charge transport. Thus, reducing the TVT content of PNDI-TVT$_x$ suppresses film crack formation and dramatically stabilizes the field-effect electron mobility upon bending (e.g., 2 mm over 2000 bending cycles). This work provides a route to tune π–π stacking in π-conjugated polymers while simultaneously promoting mechanical flexibility and retaining good carrier mobility in FOTFTs.

1. Introduction

Flexible organic thin-film transistors (FOTFTs) are a potentially important class of electronic building blocks for fabricating deformable display backplanes as well as transducers for converting mechanical signals into electrical signals for bio-sensing, health care, and robotics.[1–12] Effective FOTFT fabrication relies on several strategies, such as positioning the entire device, and particularly the most mechanically sensitive components, in the neutral plane of a multilayer architecture to alleviate mechanical stress on bending.[13–21] Another FOTFT design strategy utilizes polymeric material components with greater tolerance to mechanical stresses.[22–29] Thus, Bao et al. reported that the incorporating dynamic non-covalent crosslinking between polymer chains achieves stretchability and self-healing properties.[22] In a very different approach from our laboratory, a flexible polymeric binder was incorporated into a molecular semiconductor to plasticize grain boundaries.[10] Other very successful approaches incorporate elastomers or ionic

---

D. Zhao, G. Wang, W. Huang, T. J. Marks, A. Facchetti
Department of Chemistry and the Materials Research Center
Northwestern University
2145 Sheridan Road, Evanston, IL 60208, USA
E-mail: t-marks@northwestern.edu; afacchetti6@gatech.edu

D. Zhao, W. Huang
School of Automation Engineering
University of Electronic Science and Technology of China
Chengdu 611731, China

D. Zhao, Z. Zhu
Department of Chemistry
City University of Hong Kong
Kowloon 999077, Hong Kong

The ORCID identification number(s) for the author(s) of this article can be found under https://doi.org/10.1002/adfm.202310071

DOI: 10.1002/adfm.202310071

D. Kim
Department of Chemistry and Chemical Engineering
Chalmers University of Technology
Gothenburg SE 412 96, Sweden

S. Ghosh
Department of Chemical Engineering
Birla Institute of Technology and Science
Pilani, Rajasthan 333031, India

I. Zozoulenko
Laboratory of Organic Electronics
Linköping University
Norrköping 60174, Sweden
E-mail: igor.zozoulenko@liu.se

A. Facchetti
School of Materials Science and Engineering
Georgia Institute of Technology
Atlanta, GA 30332, USA

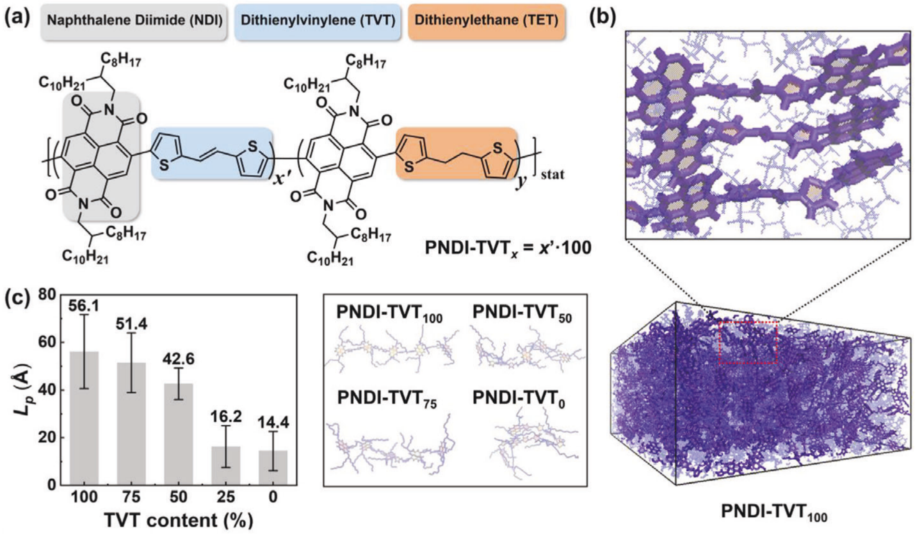

Figure 1. a) Chemical structure of the PNDI-TVT$_x$ polymer family used in this study. b) Representative snapshot of the PNDI-TVT$_{100}$ film. c) Persistence length, L_p, of polymer chains for different TVT contents, and representative snapshots illustrating polymer chain conformations as the TVT content decreases from 100% to 0% (see also Figure S1, Supporting Information).

liquids in semiconductors to enhance elasticity and preserve excellent charge transport.[30,31] Nevertheless, despite these promising approaches, there is typically a mutual exclusivity of mechanical deformability and efficient charge transport.[32–34]

Extensive π-conjugation and backbone planarity in semiconducting polymers are known to enhance macromolecule self-assembly, aggregation, and long-range packing order, yielding highly textured films and efficient charge transport, however at the expense of enhanced brittleness.[35] A few pioneering studies reported that interrupting the π-conjugation of semiconducting polymers with insulating units greatly enhances ductility for both p- and n-type conjugated polymers,[23,24,36,37] mainly by suppressing long-range crystallinity of the corresponding films. Thus, Lipomi, Mei, and co-workers developed several series of conjugation-breaking spacers to interrupt the sp^2-hybridized backbone of semiconducting polymers.[36–38] These backbone engineering strategies affected chain flexibility and backbone glass-transition temperature (T_g), properties that accompany ductility.[24] However, it would be important to better understand how variations in polymer-polymer intermolecular forces affect the response of such semiconductors under mechanical stress.[35,39,40] Especially, it would be very instructive to better understand, both from experimental and theoretical viewpoints, how interrupting π-conjugation affects the relationships between molecular structure, material flexibility, and charge transport.[41–43]

We previously reported a family of donor-acceptor naphthalenediimide (NDI)-based polymers with tunable π-conjugation lengths, referred to as PNDI-TVT$_x$ (**Figure 1**a), which were synthesized by co-polymerizing the NDI acceptor unit, *N*-functionalized with 2-octyldecyl (2OD) chains, with variable molar ratios of two different, yet lengthwise equivalent donor units consisting of the π-conjugated dithienylvinylene (TVT) and the π-nonconjugated dithienylethane (TET) comonomers. By tuning the x content where x in the TVT/TET molar ratio, = 100, 80, 60, 40, 20, 0%, and thus reducing the π-conjugation length of PNDI-TVT$_x$, the thermal, optoelectronic, and morphological properties of these semiconducting polymers vary while retaining substantial electron mobilities in (rigid) bottom-gate top-contact OTFTs.[35] Noteworthy is a significant reduction in the melting temperature (T_m) from 273 °C to 160 °C on moving from the fully conjugated ($x = 100$) to the fully non-conjugated ($x = 0$) polymer for comparable molecular masses. Interestingly, grazing-incidence wide-angle X-ray spectroscopy (GIWAXS) data indicates that all thermally annealed (150 °C) PNDI-TVT$_x$ films retain significant texturing with identical in-chain periodicity and considerable π–π stacking, independent of the degree of deconjugation. Thus, we questioned if the mechanical properties of PNDI-TVT$_x$ films will also vary with the deconjugation, whether more flexible/mechanically robust semiconductor films can be realized and how charge transport in mechanically flexible TFTs might be affected.

In this work, we investigate via both theoretical simulations and experimental characterizations the relationship between the extent of in-chain π-conjugation of PNDI-TVT$_x$ and film microstructure, mechanical properties, and charge transport characteristics. Thus, molecular dynamic simulations provide interchain radial distribution functions, inter- and intra-chain order, elastic modulus, and bonded/non-bonded interactions which are correlated with experimental data from atomic force microscopy (AFM), GIWAXS, elastic modulus, and crack onset. In addition, PNDI-TVT$_x$-based FOTFTs are fabricated to quantify charge transport on a flexible platform and the mechanical stress tolerance as a function of in-chain π-conjugation. The data demonstrate that such simulations can provide predictive models in quantitative agreement with experimental observations.

2. Results and Discussion

In this section we first investigate the strength of interchain interactions and packing in PNDI-TVT$_x$, and how they affect chain conformation and mechanical properties, by molecular dynamic

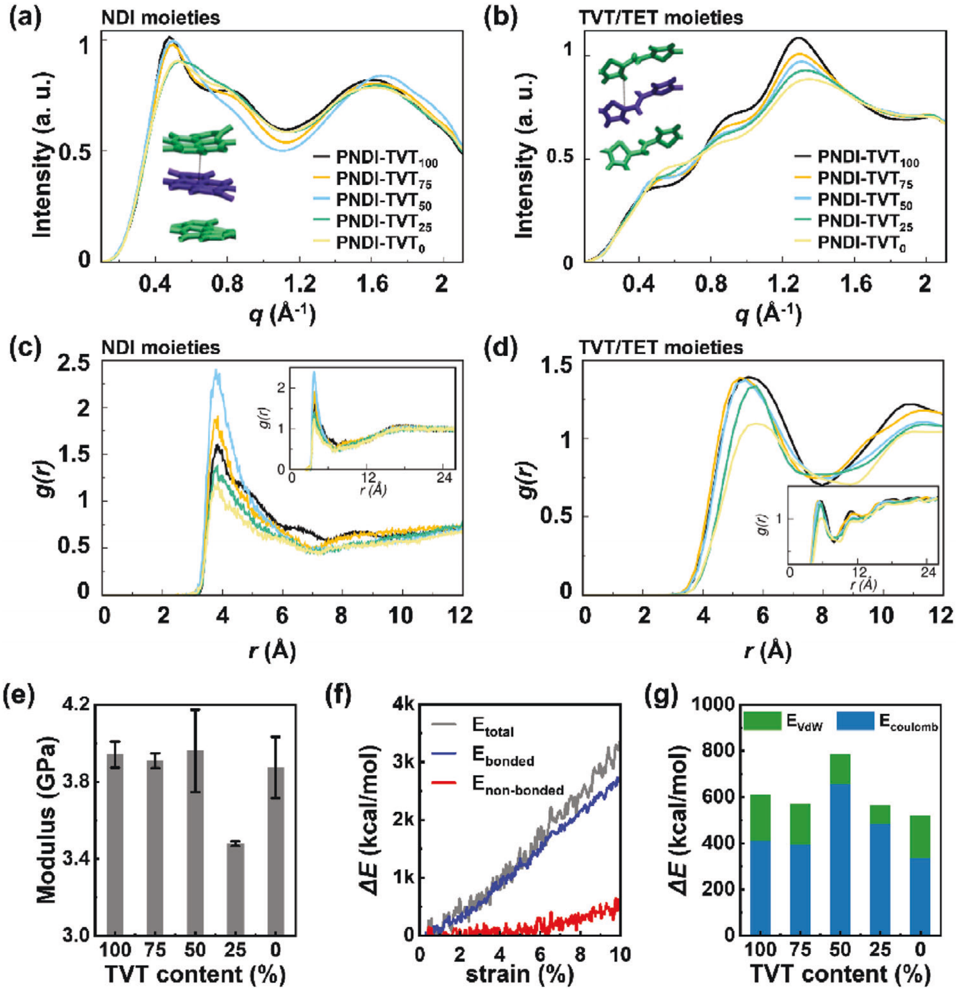

Figure 2. MD simulation-derived XRD plots for a) NDI moieties and b) TVT/TET moieties. MD simulation-derived interchain radial distribution functions for c) NDI and d) TVT/TET moieties. e) Computed elastic modulus obtained from MD simulations. f) Simulated change in total (E_{total}), bonded (E_{bond}) and non-bonded ($E_{\text{non-bonded}}$) energies for PNDI-TVT$_0$ during deformation. g) The change in Van der Waals (E_{VdW}) and Coulombic (E_{coulomb}) energies of PNDI-TVT$_x$ films when a strain of 3% is applied.

(MD) simulations. Next, we correlate the computed data with experimental morphological and mechanical properties results. Finally, we access the charge transport of these polymers by fabricating FOTFTs and how it changes upon mechanical deformation and TVT/TET content.

2.1. Molecular Dynamic Simulations

To understand the film morphology and the mechanical response of PNDI-TVT$_x$ films to strain, and how they vary with x, we carried out MD simulations. For all calculations a polymer chain is modelled by five NDI moieties, *N*-functionalized with 2OD chains, alternated by four TVT/TET moieties, with $x = 100, 75, 50, 25, 0$. These calculations, comprising 150 polymer chains, allow analysis of the PNDI-TVT$_x$ film morphology, the evolution of the interchain π–π stacking, the persistence length (L_p) and the end-to end distance (d_e) of the polymer chains as the TVT content decreases. The persistent length defines the length over which the correlation between the chain orientations is lost and therefore correlates with the polymer chain stiffness.[44–46] Figure 1b,c reports representative snapshots of computed polymer chain conformations and bulk morphologies without the substrate as well as L_p of the PNDI-TVT$_x$ series while d_e and its distribution for different TVT contents are shown in Figure S1 (Supporting Information). Clearly both L_p and d_e of PNDI-TVT$_x$ decrease as x decreases, indicating that enhancing deconjugation (TET content) reduces the bending stiffness of the polymer chains. This result mainly originates from the decreased fraction of π-conjugated bonds in the polymer backbone enhancing backbone conformational freedom.[18]

To better understand the effect of the TVT/TET content on the film morphology of PNDI-TVT$_x$, the X-ray diffraction (XRD) patterns (**Figure 2**a,b) and the interchain radial distribution function [$g(r)$, Figure 2c,d] were computed. Note, these are two separate sets of computations (see Experimental section and Supporting Information for details). The interchain $g(r)$ provides the probability to find a NDI (or TVT/TET) unit at the distance r from a NDI (or TVT/TET) unit on the nearby chain without considering the periodicity within the chain. From the XRD patterns, which account for both intra- and inter-chain periodicities, the stacking distance *r* was calculated from the relation $r = 2\pi/q$.[47] The simulated XRD patterns of the NDI moieties for all TVT contents (Figure 2a) exhibit a broad peak at $q \approx 1.6$ Å^{-1}, which corresponds to a π-π stacking distance of ≈3.8 Å for the NDI moieties (Table S1, Supporting Information). Here, the peak in the range of ≈0.4–0.6 Å^{-1} arises from the lamellar stackings among the chains and periodicity of the NDI moieties within the chain. The above-mentioned peak is at ≈0.45 Å^{-1} (r = ≈14 Å) for x = 100, 75 and 50 and shifts to ≈0.52 Å^{-1} (r = ≈12 Å) for $x = 25$ and 0. The decrease in the distance is due to incorporation of more flexible TET moieties in the backbone which reduces the bending stiffness of the chain. As shown in Figure 2c and Table S2 (Supporting Information), the inter-chain distribution function $g(r)$ of the NDI moieties also exhibits a pronounced peak at ≈3.8 Å corresponding to the π–π stacking distance between two NDI moieties (see inset of Figure 2a). The calculated $g(r)$ intensity for the interchain NDI moieties with the TVT content varies in the following order: 50% (2.40) > 75% (1.90) > 100% (1.6) > 25% (1.35) > 0% (1.15) (see Figure 2c) and thus maximizes for PNDI-TVT$_{50}$ (2.40) and is the lowest for PNDI-TVT$_0$ (1.15). Interestingly, the interchain distribution of NDI moieties suggests that the greatest π–π stacking is achieved for an intermediate TVT content in this polymer series.

Next, we discuss the change in morphology of PNDI-TVT$_x$ films with respect to the TVT/TET moiety content. The simulated XRD patterns of the TVT/TET moieties exhibit a peak ranging over ≈1.2–1.4 Å^{-1} (Figure 2b) corresponding to an interchain stacking distance of the TVT/TET moieties of ≈4.5–5.1 Å. The corresponding interchain $g(r)$ (Figure 2d) exhibits a pronounced peak at almost the same distances, and the intensity monotonically falls as the TVT content falls [100% (1.39) > 75% (1.38) > 50% (1.37) > 25% (1.32) > 0% (1.09)]. Note, the interchain stacking distance between thiophene-containing moieties increases more for lower TVT content (see, $x = 0$ and 25). These data correlate with the greater decrease in $g(r)$ intensity, and thus in overall crystallinity of these polymers and is also in accord with the decrease in interchain π-π stackings of NDI moieties. Note, upon reducing the TVT content to 20% and 0% the backbone becomes very flexible and the chains fold, resulting in the appearance of intrachain π-π stackings (see Figure 1c and more detail in Figure S2, Supporting Information). The $g(r)$ for TVT/TET moieties including the periodicity within the chains is plotted in Figure S3 (Supporting Information), which reveals an increase in intrachain π–π stackings with decreasing the TVT content. The first peak in the $g(r)$ plot at ≈4 Å has the major contributions from the periodicity of the thiophene rings within the chain which represents intrachain π–π stacking between the thiophene rings of TVT/TET moieties. The second peak in the $g(r)$ plot at 6.30 Å is due to the periodicity of two adjacent thiophene rings within the chain. The intensity of the first peak is increasing with decreasing the TVT content due to the increase in intrachain π–π stackings. In contrast, the intensity of the second peak decreases with TVT content due to the enhanced chain flexibility, which translates to chain folding and increased intrachain π–π stackings. There is also a slight leftward shift in the second peak from 6.30 to 6.15 Å as the rigid —CHCH— units are replaced by flexible —CH$_2$—CH$_2$— unites that in turn compresses the distance between two thiophene rings as the TVT content falls. Therefore, our computations argue that at higher TVT contents the film crystallinity is high due to predominant interchain stackings which are significantly reduced at lower TVT contents. At the intermediate TVT content (50%), the rigid TVT moieties allow substantial retention of interchain π–π stacking while the flexible TETs enhance intrachain π-π stacking, further increasing texturing. The overall result of these computations suggests that PNDI-TVT$_x$ polymers with intermediate x values should exhibit the greatest crystallinity.

2.2. Simulated Mechanical Properties

We also computed the elastic modulus of the PNDI-TVT$_x$ films and, as shown in Figure 2e and Table S3 (Supporting Information), find relatively small variations for different TVT contents. Thus, the computed modulus first decreases from 3.94 ± 0.07 to 3.91 ± 0.04 GPa as the TVT content falls from 100% to 75%, then increases as to 3.96 ± 0.21 GPa for a 50% TVT content, and finally falls to 3.48 ± 0.01 and 3.87 ± 0.16 GPa for the lowest TVT contents of 25 and 0%. Note that these data correlate better with the variation of $g(r)$ of the NDI units rather than L_p. In addition, we can use MD simulations to identify the contributions of the bonded and non-bonded interactions to the elastic modulus by computing the total energy (E_{total}), which is given by the sum of the non-bonded energy ($E_{non\text{-}bonded}$), bonded energy (E_{bonded}) and kinetic energy ($E_{kinetic}$) according to $E_{total} = E_{bonded} + E_{non\text{-}bonded} + E_{kinetic}$. Note, $E_{non\text{-}bonded}$ is a sum of van der Waals and Coulombic energies, and E_{bonded} is a sum of the bond angle, and dihedral energies resulting from the covalent bonding between atoms. Since the change of $E_{kinetic}$ during deformation is negligible compared to the potential energy (E_{bonded} and $E_{non\text{-}bonded}$), $E_{kinetic}$ is omitted in Figure 2f. Thus, in the case of PNDI-TVT$_0$ film while both E_{bonded} and $E_{non\text{-}bonded}$ increase with application of the tensile strain, the contribution of $E_{non\text{-}bonded}$ to E_{total} is much larger than E_{bonded}, indicating that the non-bonded interactions, specifically, the change in van der Waals interactions is dominant during deformation. As shown in Figure 2g, the case of all PNDI-TVT$_x$ films van der Waals interactions between chains, mainly originating from π–π stacking, play an important role in the elastic modulus of these films.

2.3. Film Morphology and Microstructure

Experimental film morphology and microstructure were assessed by AFM and GIWAXS. As shown in **Figure 3**a, all spin-coated PNDI-TVT$_x$ films on Si/SiO$_x$ (300 nm) substrates and annealed at 120 °C exhibit an interconnected and fibrillar morphology in the AFM. However, the film surface fibrillar structure, and thus the surface root-mean-square roughness (σ_{RMS}), varies significantly when the TVT content decreases. Thus, PNDI-TVT$_x$ films with the x from 100 to 40 are relatively smooth and σ_{RMS} monotonically increases from 2.8 nm (100%) to 3.8 nm (60%) to 4.1 nm (40%). However, the film morphology of PNDI-TVT$_x$ with the TVT content of 20% and 0% evidence large and randomly oriented domains and are characterized by a very large σ_{RMS} of 8.7

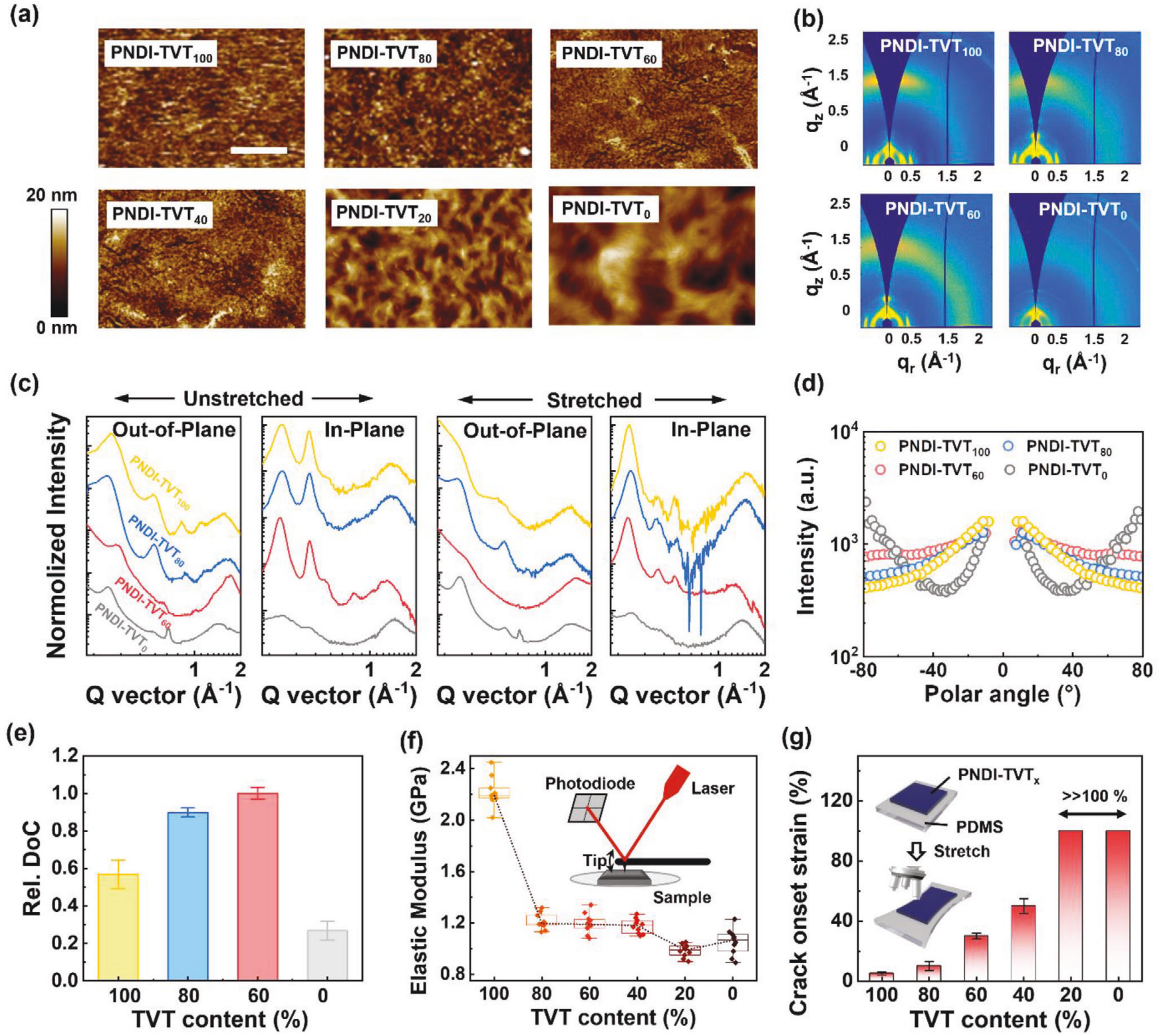

Figure 3. a) AFM height images of PNDI-TVT$_x$ films. b) GIWAXS of the indicated PNDI-TVT$_x$ unstretched films. c) The corresponding 1D GIWAXS line profiles taken along the out-of-plane and the in-plane scattering directions. d) Pole figures calculated from (010) peaks at 0.27 Å^{-1} for unstretched films. e) Plot of the relative degree of crystallinity of the PNDI-TVT$_x$ films obtained by integrating the pole figures. f) Experimental elastic modulus measured by AFM tipping model. g) Schematic image of the crack onset strain measurement setup and crack onset strain of PNDI-TVT$_x$ films.

and 10.2 nm, respectively. Furthermore, the fibrillar structures of the former films are better defined and exhibit a certain degree of alignment. Interestingly, the σ_{RMS} results correlate with the L_p of the PNDI-TVT$_x$ series in Figure 1c, suggesting that decreasing the TVT content in the backbone reduces chain alignment. Also note that poorer AFM image quality of the PNDI-TVT$_0$ and PNDI-TVT$_{20}$ films using the same force-constant AFM probe tip implies "softer" samples.[37]

Additionally, the PNDI-TVT$_x$ film microstructure as the TVT content was decreased for both the pristine and 80% uniaxially strained samples was characterized by GIWAXS. For these measurements the polymers films were first transferred from OTS-modified Si/SiO$_x$ wafers to polydimethylsiloxane (PDMS) substrates, next stretched, and finally transferred back to the Si substrates. The role of OTS-modification is to reduce the adhesion of the polymer film to the wafer and thus facilitate the transfer process. As shown in the 2D GIWAXS patterns of Figure 3b, all unstretched films are textured, in agreement with our previous investigation for films fabricated on Si substrates.[35] The out-of-plane (OoP) and in-plane (IP) 1D sector-averaged profiles obtained from the OoP and IP sectors of the unstretched films are shown in the left of Figure 3c. For all samples, the PNDI-TVT$_x$ (n00) lamellar and (010) π–π stacking reflections are evident in both OoP and IP directions, suggesting the presence of π-face-on as well as π-edge-on populations in the ordered domains. From this dataset some interesting trends are observed. Where the (100) reflections along OoP are similar for all TVT contents [q (Å^{-1}) = 0.27–0.28] except for the 60% (0.30 Å^{-1}), the IP reflections are pinned at q = 0.26 Å^{-1}for all polymer samples. Thus, the lamellar periodicity (d_{lam}) is the shortest for PNDI-TVT$_{60}$ (20.93 Å) while those of all other polymers in the OoP direction are 22.42–23.27 Å and those in the IP direction are pinned at 24.15 Å. Regarding the (010) π–π stacking reflection, when the TVT content decreases the reflection initially increases and then decreases along OoP [q (Å^{-1}) = 1.58 (100%), 1.60 (80%), 1.62 (60%), 1.57 (0%)] while it falls to lower values, and exhibits an opposite trend, along IP [q (Å^{-1}) = 1.54 (100%), 1.54 (80%), 1.51 (60%), 1.55 (0%)]. Thus, in the OoP direction, first a significant compression of the π–π stacking periodicity (d_π) from 3.98 to 3.88 Å is observed when the TVT content is reduced from 100% to 60% and then it increases considerably for the non-conjugated polymer (4.00 Å for TVT = 0%). The d_π trend agrees with the calculated distances between NDI moieties in Table S4 (Supporting Information). In the IP direction, as for d_{lam}, the d_π varies in a opposite trend (d_π of 50% < 75% < 100% < 25% < 0%) and to a lesser degree [d_π (Å) = 4.08 (100%), 4.08 (80%), 4.16 (60%), 4.05 (0%). Note, we have not measured the XRD of these films but accessed their microstructure by GIWAXS experiments (vide infra).

The calculated pole figures for the (010) reflection (Figure 3d) represent the orientational distribution of the polymer crystallites with respect to the surface normal after conversion of detector azimuth to the crystal polar angle (ω). For a consistent comparison, the relative degree of crystallinity (rDoC) of the PNDI-TVT$_x$ films was calculated from pole figures by integrating the intensities of the (010) reflection over the crystallographic orientation sphere: $\text{DoC} = \int_{0^\circ}^{90^\circ} I(\omega) \sin \omega d\omega$. As shown in Figure 3e, the rDoC first increases when the TVT content falls from 100% to 60% then drops precipitously by the fully deconjugated PNDI-TVT$_0$. These data reflect the trends identified in the MD-derived $g(r)$ data for the π–π stacking peak of the NDI moieties, and are thus the best descriptor of the polymer crystallinity, while the distances between NDI units from the XRD simulation best represent the intermolecular correlations between backbones.

When the present films are stretched to 80% strain, the intensity of most OoP reflections, particularly those associated with the lamellar spacings, fall significantly (Figure 3c, right) while for the IP direction one remains strong but with an altered relative strength within the (n00) reflection family. Therefore, uniaxial stretching of these films affects OoP crystallinity much more than IP texturing. The result is a change in the rDoC of these samples after stretching (Figures S4 and S5, Supporting Information) where PNDI-TVT$_{100}$ and PNDI-TVT$_0$ are the most and, by far, the least textured films while the polymers with the intermediate TVT content have intermediate rDoC values. However, all reflection peak positions, and thus both d_{lam} and d_π in both OoP and IP directions exhibit negligible variations under stretching, thus the trends of these parameter upon stretching hold.

From the overall computed and experimental PNDI-TVT$_x$ morphological analysis, it is evident that when the TVT content is very high, the chains are too stiff to reorganize efficiently in the solid state at the modest temperature used in the film fabrication (≈120 °C). Thus, while close π–π stacking occurs the crystalline domain sizes are nonoptimal. In contrast, for the nonconjugated polymer, the chains are too flexible for efficient intermolecular organization. Polymers with mid-TVT contents have semi-rigid chains which can fold, resulting in strongly packed π–π stack segments as well as the formation of larger crystalline domains. This morphological picture suggests that polymers with an intermediate TVT content should offer the optimum compromise between efficient charge transport and mechanical deformation stability.

2.4. Experimental Mechanical Properties

The elastic moduli of PNDI-TVT$_x$ polymers with a TVT/TET content of 100 to 80, 60, 40, 20, and 0% were measured by AFM modulus mapping.[32–34] As shown in Figure 3f and Table S5 (Supporting Information), the PNDI-TVT$_x$ elastic modulus trend generally tracks that of the computed values with the largest values for PNDI-TVT$_{100}$ (2.20 ± 0.25 GPa), the lowest values for PNDI-TVT$_x$ with low TVT contents: 0% (1.08 ± 0.15 GPa) > 20% (0.98 ± 0.07 GPa), and intermediate values for other contents, 60% (1.22 ± 0.12 GPa) > 80% (1.20 ± 0.07 GPa) > 40% (1.19 ± 0.08 GPa). Despite the similar trends, the measured PNDI-TVT$_{100}$ modulus is substantially larger than those of the other PNDI-TVT$_x$ polymers, which is not the case for the computed values. This difference may originate from the fact that the calculations were performed for the bulk films without a contribution from the substrate, which is known to be important for describing the morphology of semiconducting polymers.[48] Thus, additional MD simulations for a PNDI-TVT$_{100}$ film on a silicon substrate were carried out to better model the experimental samples (Figures S5 and S6, Supporting Information). Interestingly, we find subtle elastic modulus differences between out-of-plane and in-plane computations, and regardless of the deformation direction, elastic modulus of the system with substrate included is curiously lower than that of the free-standing films. Thus, another possible reason for the disparity between the experimental and simulated PNDI-TVT$_{100}$ film elastic moduli may originate in choosing relatively short chain lengths for the simulation. Particularly for PNDI-TVT$_x$ with a large TVT content, the rigid short chains in the film may slip more easily during deformation simulations, leading to a lower modulus. This hypothesis is supported by the disappearance of the PNDI-TVT$_{100}$ π–π stacking peak in the simulation during deformation, as shown in Figure S8 (Supporting Information). Future studies will address calculations of film morphology and the elastic moduli of PNDI-TVT$_x$ films with longer chains which will require coarse-grained simulations of much larger systems.

Finally, the crack onset strain of these polymers was also accessed by optical microscopy for PNDI-TVT$_x$ films transferred to PDMS substrates (Figure 3g and Figures S8–S13, Supporting Information) and the data are also collected in Table S5 (Supporting Information).[23] Thus, the crack onset strain monotonically increases as the TVT content decreases in the order: 5±1% (PNDI-TVT$_{100}$), 10 ± 3% (PNDI-TVT$_{80}$), 29 ± 2% (PNDI-TVT$_{60}$), 51 ± 5% (PNDI-TVT$_{40}$), and >100% (PNDI-TVT$_0$ and PNDI-TVT$_{20}$), the latter measurement equipment limited. This result indicates that while the differences in elastic properties among these polymers

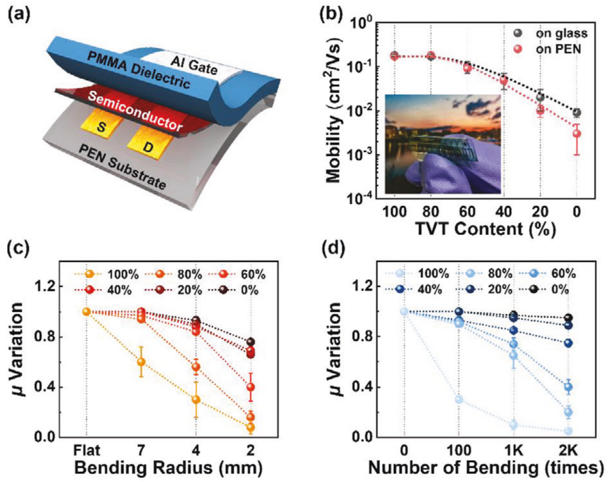

Figure 4. a) Top-gate/bottom-contact FOTFT structure used in this study to quantify charge transport of the PNDI-TVT$_x$ polymers. b) Electron mobility of PNDI-TVT$_x$ FOTFTs with various TVT contents before bending. c) Electron mobility variations of PNDI-TVT$_x$ FOTFTs upon deformation along the L channel direction at different bending radii. d) Electron mobility variations of PNDI-TVT$_x$ FOTFTs upon bending the devices along the L channel direction at 7 mm bending radius for different times.

is limited, the plastic deformation increases dramatically with falling TVT content, reflecting the stepwise deconjugation. Interesting, if we replace TVT with bithiophene in PNDI-TVT$_{100}$, the resulting polymer is N2200 [also called P(NDI2OD-T2)], which is a well-known and widely studied semiconductor exhibiting an electron mobility between 0.1 to 6 cm^2 V^{-1} s^{-1}.[49–51] The mechanical properties of N2200 films and OTFTs have been investigated to a certain extent as pristine, blended, and encapsulated films.[20,51,52] For instance, Kim et al. reported tensile behavior of ≈100 nm thick N2200 films based on polymer batches with different molecular masses. It was found that the batches with molecular weight/ polydispersity index of 49 kDa/2.60 (similar to PNDI-TVT$_{100}$, 51 kDa/2.33) and 163 kDa/2.42 exhibit an elastic modulus/crack onset of 0.74 ± 0.04 GPa/1.1% (vs 2.20 ± 0.25 GPa/5 ± 1% for PNDI-TVT$_{100}$) and 0.92 ± 0.02 GPa/34.2%, respectively.[49] Thus, again, while the elastic modulus remains in a narrow range, the crack onset strongly depends on the structure as well as the molecular mass, making a direct correlation of the mechanical properties upon co-monomer replacement difficult when accessed in different laboratories.

2.5. FOTFTs and Charge Transport upon Mechanic Deformation

Charge transport measurements were carried out both on rigid (glass) and flexible (polyethylene naphthalate, PEN) substrates and, for the latter, upon bending the devices at different radii. The device structures were, glass or PEN (substrate)/Au (source-drain)/PNDI-TVT$_x$/PMMA (dielectric)/Al (gate) (**Figure 4**a). Note that rigid TFTs on glass were fabricated here since in our previous study the PNDI-TVT$_x$ films were annealed at 150 °C.[35] Because PEN has limited thermal stability at this temperature,[2] all PNDI-TVT$_x$ films here were necessarily processed at 120 °C to allow direct performance comparison between the rigid and flexible platforms. The semiconducting layer was deposited by spin-coating a polymer solution in toluene (5 mg mL^{-1}). All devices were fabricated in an argon-filled-glovebox and evaluated under ambient conditions. Performance parameters, including field-effect mobility (μ), were extracted using standard MOSFET equations.[53]

As expected, the field-effect electron mobility (μ_e) of the rigid (glass) OTFTs fabricated here are lower than those measured previously for the semiconductor films annealed at a higher temperature,[35] however, the trend is identical (Figure 4b and Figure S15 and Table S6, Supporting Information). Thus, as the TVT content decreases from 100 to 60%, the mobility first remains in a narrow range, 0.18 ± 0.02 cm^2 V^{-1} s^{-1} (100% and 80%) and 0.10 ± 0.03 cm^2 V^{-1} s^{-1} (60%), then falls to 0.05 ± 0.01 cm^2 V^{-1} s^{-1} (40%) and 0.02 ± 0.01 cm^2 V^{-1} s^{-1} (20%), and finally remains non-negligible for the fully deconjugated polymer, 0.009 ± 0.002 cm^2 V^{-1} s^{-1} (0%). Importantly, the mobilities of FOTFTs on PEN, μ_e (cm^2 V^{-1} s^{-1}) = 0.17 ± 0.02 (100%), 0.18 ± 0.02 (80%), 0.10 ± 0.02 (60%), 0.05 ± 0.01 (40%), 0.010 ± 0.003 (20%), and 0.003 ± 0.002 (0%), are almost identical to those of the rigid devices on glass, with all exhibiting negligible I–V hysteresis (Figure 4b and Figure S16 and Table S7, Supporting Information).

Next, we evaluated how PNDI-TVT$_x$ charge transport is affected when bending the FOTFTs at a radius from ∞ to 2 mm, parallel to the charge transport direction (Figures S17–S20, Supporting Information). The strain during the film bending process is calculated by the deformation quantity of semiconductor layer relative to the neutral layer.[10] As shown in Figure 4c and Table S8 (Supporting Information), the μ_e variation upon bending depends significantly on the TVT monomer content. Upon bending the PNDI-TVT$_{100}$ devices at a radius of , 4 mm, and 2 mm, the electron mobility decreases substantially from 0.17 ± 0.02 cm^2 V^{-1} s^{-1} to 0.10 ± 0.01 cm^2 V^{-1} s^{-1} (mobility reduction of ≈40%), to 0.05 ± 0.03 cm^2 V^{-1} s^{-1} (≈70%) and 0.008 ± 0.001 cm^2 V^{-1} s^{-1} (≈95%), respectively. However, incorporation of TET in the PNDI-TVT$_x$ films significantly reduces mobility depression, particularly at 7 mm for all devices and at all bending radii for those with greater TET contents. Thus, the PNDI-TVT$_{80}$ and PNDI-TVT$_{60}$ FOTFTs exhibit a moderate mobility decrease of ≈5% (from 0.18 ± 0.03 to 0.17 ± 0.01 cm^2 V^{-1} s^{-1}) and ≈3% (from 0.10 ± 0.02 to 0.097 ± 0.003 cm^2 V^{-1} s^{-1}) at 7 mm, ≈50% (0.09 ± 0.02 cm^2 V^{-1} s^{-1}) and ≈16% (0.084 ± 0.01 cm^2 V^{-1} s^{-1}) at 4 mm, and ≈83% (0.028 ± 0.003 cm^2 V^{-1} s^{-1}) and ≈40% (0.041 ± 0.005 cm^2 V^{-1} s^{-1}) at a 2 mm radius, respectively. Importantly, the PNDI-TVT$_{40}$, PNDI-TVT$_{20}$ and PNDI-TVT$_0$ devices exhibit a far lower mobility reduction of <10% at 7 nm, <20% at 4 mm, and <30% after bending tests at a 2 mm radius.

Finally, repeated bending tests were performed for PNDI-TVT$_x$ devices at 7 mm over 0 to 2000 bending cycles (Figure 4d and Table S9, Supporting Information) and it is found that the magnitude of device performance degradation decreases as the TVT content decreases. Thus after 2000 bending cycles at a 7 mm radius, the μ_e of PNDI-TVT$_{100}$, PNDI-TVT$_{80}$, and PNDI-TVT$_{60}$ falls by ≈95% (from 0.17 ± 0.02 to 0.008 ± 0.001 cm^2 V^{-1} s^{-1}), ≈80% (from 0.18 ± 0.03 to 0.036 ± 0.003 cm^2 V^{-1} s^{-1}) and ≈60% (from 0.10 ± 0.02 to 0.041 ± 0.005 cm^2 V^{-1} s^{-1}), respectively. Compared with these results, a far lower μ_e decline occurs after 2000 cycle bending cycles for PNDI-TVT$_{40}$, PNDI-TVT$_{20}$, and PNDI-TVT$_0$, which falls by only ≈15% (from 0.05 ± 0.01 to 0.043 ± 0.002 cm^2 V^{-1} s^{-1}), ≈10% (from 0.010 ± 0.001 to 0.009 ± 0.002 cm^2 V^{-1} s^{-1}), and ≈5% (from 0.0032 ± 0.001 to 0.003 ± 0.001 cm^2 V^{-1} s^{-1}), respectively. These results are in accord with the mechanical plastic deformations trends and film texturing observed for the semiconducting polymer film (vide supra).

3. Conclusions

We demonstrated here that progressively reducing the content of the π-conjugated monomer TVT with respect to the nonconjugated co-monomer TET in the PNDI-TVT$_x$ semiconducting polymer series enables progressive modulation of the macromolecular structure, chain rigidity, morphological response to strain, and charge transport properties as assessed from concurring MD simulations and experimental results. To understand the effect of TVT content on inter- and intra-chain interactions, the $g(r)$, XRD, elastic modulus, and bonded/non-bonded interactions were first computed by MD. Although the simulations and experiments differ, particularly for the modulus of PNDI-TVT$_{100}$, the general trends are reproduced indicating that decreasing the TVT content in these polymers, the interchain distance between NDI moieties/backbone, π–π stacking, van der Waals interactions, and texturing are optimal at an intermediate TVT content. Furthermore, our experimental data indicate that lowering the TVT content does not dramatically affect the elastic behavior but strongly affects plastic deformation (crack onset), which falls monotonically when the TVT content falls, which correlates with the T_g and the computed chain bending stiffness in this polymer series. Finally, FOTFTs based on the present PNDI-TVT$_x$ films illustrate the effects of conjugation length on the electron mobility, with PNDI-TVT$_{60}$ delivering the optimum performance balance between mechanical flexibility and mobility. We believe that this combined experimental and computational study will guide the design of future π-conjugated building blocks to further enhance FOTFT performance and stretchability.

4. Experimental Section

Materials, Films and Device Fabrication, and Characterization: PNDI-TVT$_x$ were synthesized and purified according to the previous procedure.[35] All solvents were purchased from Sigma-Aldrich and used as received. The PEN substrate film had a thickness of 130 µm. PMMA (120 kDa) was purchased from Sigma-Aldrich. The n^{++} silicon wafer substrates with a 300 nm thick silicon dioxide were cut into 2 cm × 2 cm squares. All OTFTs have a top-gate-bottom-contact architecture. PEN substrates were cleaned ultrasonically with isopropyl alcohol and oxygen plasma. For both rigid substrates, 25 nm thick gold source/drain electrodes were deposited by thermal evaporation at a pressure of 5 × 10^{-6} Torr though a shadow mask (channel width = 1000 µm and channel length = 50 µm). For semiconductor deposition, the PNDI-TVT$_x$ polymers were dissolved in anhydrous toluene at a 5 mg mL^{-1} concentration. The semiconductor solutions were filtered through a 0.2 µm polytetrafluoroethylene (PTFE) filter and spin-coated at 1000 rpm for 30 s in a N$_2$ filled glove box. These films were then annealed at 120 °C for 30 min in the glove box. Next, the PMMA dielectric solution (70 mg mL^{-1} in 2-butanone) was spin-coated at 1500 rpm for 40 s on the semiconduction polymer films and annealed at 80 °C for 3 h under N$_2$. Finally, the FOTFTs were completed by depositing Al top-electrodes (50 nm) by thermal evaporation. For all devices, electrical characterization was performed in ambient and in the dark on a custom probe station using an Agilent 1500 semiconductor parameter analyzer. AFM images were collected with a Bruker atomic force microscope (Dimension) in tapping mode. Optical micrographs were acquired on a Nikon Model Eclipse Ci-L optical microscope. GIWAXS measurements were performed at beam-Line 8ID-E at the Advanced Photon Source at Argonne National Laboratory.

Molecular Dynamics Simulations on PNDI-TVT$_x$: A total of 150 polymer chains were used in all simulations. The morphology of the PNDI-TVT$_x$ was studied using a LAMMPS molecular dynamics simulation package.[54] The initial systems were generated in Moltemplate,[55] and the size of the initial computational box was 30 × 30 ×15 nm^3. The box was quickly deformed to 18 × 18 × 9 nm^3 to achieve a density that is approximately closer to the actual density. The bonded and nonbonded interactions of the polymers were defined by the general AMBER force field as implemented in the Moltemplate. The simulations were run in the isothermal isobaric (NPT) ensemble with a time step of 1 fs. The effect of solvent was implicitly modeled by Langevin dynamics with a damping parameter of 3800 fs and a dielectric constant of 5. The film was first equilibrated at 800 K for 10 ns, then it was quenched from 800 K to 300 K at a cooling rate of 20 K per ns and during the quench procedures, after each 20 K temperature drop, i.e., after each ns run, the system was equilibrated for 0.5 ns. Finally, the system was again equilibrated at 300 K during 2.5 ns. The pressure was kept constant at 1 atm. The Coulomb interaction was calculated using via particle–particle particle–mesh solver with a cutoff of 1 nm.[56] Interchain radial distribution function $g(r)$ of the rings present in the polymer chains was calculated using the following equation,

$$g\ (r) = \frac{N}{\frac{4}{3}\pi\left[(r+\delta r)^3 - r^3\right]} \times \frac{1}{\rho_{\text{bulk}}} \tag{1}$$

where, N is the number of particles present in a bin, r is the distance between two centers of mass of the rings, δr is the bin width and ρ_{bulk} is the bulk density of the system. $g(r)$ of the rings presents in the NDI moieties and $g(r)$ of the rings present in TVT/TET moieties are calculated separately. XRD pattern was calculated in LAMMPS. The persistence length of the polymer chains was calculated as shown in Figure S22 (Supporting Information).[57]

Elastic Modulus and Film Deformation Simulations: Uniaxial tensile strain was imposed to two principal axes of the film that are perpendicular to the film thickness direction at a strain rate of 1 × 10^9 s^{-1} to estimate elastic modulus of films using “fix deform” command as implemented in LAMMPS. The film deformation simulations were carried out with 1.0 fs timestep. All deformation simulations were conducted in the NPT ensemble at 300 K while the pressure of two cell faces that are perpendicular to the tensile strain direction was kept constant (anisotropic pressure control). The stress tensor corresponding to the test direction was calculated via the kinetic energy contribution and the virial contribution. The elastic modulus was estimated by calculating the slope of a line fitted to the elastic region of the stress-strain curve. Note that two elastic moduli (i.e., two strain curves) were independently calculated by deforming the film along x and y axes separately, and the calculated results for the elastic moduli (Figure 2e) show their averaged values and corresponding standard deviations.

Supporting Information

Supporting Information is available from the Wiley Online Library or from the author.

Acknowledgements

D.Z., D.K., and S.G. contributed equally to this work. A.F. and T.J.M. gratefully acknowledge financial support by AFOSR grant FA9550-22-1-0423, Northwestern University MRSEC grant NSF DMR-1720139, U.S. Department of Commerce, National Institute of Standards and Technology as part of the Center for Hierarchical Materials Design (CHiMaD) award

70NANB19H005. This work made use of the Northwestern University Micro/Nano Fabrication Facility (NUFAB), EPIC facility, Keck-II facility, and SPID facility of the NUANCE Center at Northwestern University, which is partially supported by Soft and Hybrid Nanotechnology Experimental (SHyNE) Resource (NSF ECCS-1542205), the Materials Research Science and Engineering Center (DMR-1720139), the State of Illinois, and Northwestern University. Use of the Advanced Photon Source, an Office of Science User Facility operated for the US DOE Office of Science by Argonne National Laboratory, was supported by the US DOE under Contract DE-AC02-06CH11357. A.F. acknowledges support from NSF DMR-2223922. I.Z. acknowledges support of Swedish Research Council (VR) via grant 2016-05990. S.G. acknowledges the support of SERB start-up research grant, file no SRG/2021/002169. The computations were performed on resources provided by the Swedish National Infrastructure for Computing (SNIC) at NSC and HPC2N.

Conflict of Interest

The authors declare no conflict of interest.

Data Availability Statement

The data that support the findings of this study are available in the Supporting Information of this article.

Keywords

de-conjugation, flexible organic thin-film transistors, molecular dynamics simulation, π-conjugated, π–π stacking

Received: August 23, 2023
Revised: October 2, 2023
Published online:

---

[1] J. Chen, W. Huang, D. Zheng, Z. Xie, X. Zhuang, D. Zhao, Y. Chen, N. Su, H. Chen, R. M. Pankow, Z. Gao, J. Yu, X. Guo, Y. Cheng, J. Strzalka, X. Yu, T. J. Marks, A. Facchetti, *Nat. Mater.* **2022**, *21*, 564.
[2] V. N. Le, J. H. Bombile, G. S. Rupasinghe, K. N. Baustert, R. Li, I. P. Maria, M. Shahi, P. Alarcon Espejo, I. McCulloch, K. R. Graham, C. Risko, A. F. Paterson, *Adv. Sci.* **2023**, *10*, 2207694.
[3] K. Jiang, S.-H. Hong, S.-H. Tung, C.-L. Liu, *J. Mater. Chem. A* **2022**, *10*, 18792.
[4] A. Liu, H. Zhu, S. Bai, Y. Reo, M. Caironi, A. Petrozza, L. Dou, Y.-Y. Noh, *Nat. Electron.* **2023**, *6*, 559.
[5] V. Orts Mercadillo, K. C. Chan, M. Caironi, A. Athanassiou, I. A. Kinloch, M. Bissett, P. Cataldi, *Adv. Funct. Mater.* **2022**, *32*, 2204772.
[6] A. F. Paterson, S. Singh, K. J. Fallon, T. Hodsden, Y. Han, B. C. Schroeder, H. Bronstein, M. Heeney, I. Mcculloch, T. D. Anthopoulos, *Adv. Mater.* **2018**, *30*, 1801079.
[7] S. T. Keene, J. E. M. Laulainen, R. Pandya, M. Moser, C. Schnedermann, P. A. Midgley, I. McCulloch, A. Rao, G. G. Malliaras, *Nat. Mater.* **2023**, *22*, 1121.
[8] T. Zou, H.-J. Kim, S. Kim, A. Liu, M.-Y. Choi, H. Jung, H. Zhu, I. You, Y. Reo, W.-J. Lee, Y.-S. Kim, C.-J. Kim, Y.-Y. Noh, *Adv. Mater.* **2023**, *35*, 2208934.
[9] S. N. Afraj, C.-C. Lin, A. Velusamy, C.-H. Cho, H.-Y. Liu, J. Chen, G.-H. Lee, J.-C. Fu, J.-S. Ni, S.-H. Tung, S. Yau, C.-L. Liu, M.-C. Chen, A. Facchetti, *Adv. Funct. Mater.* **2022**, *32*, 2200880.
[10] D. Zhao, J. Chen, B. Wang, G. Wang, Z. Chen, J. Yu, X. Guo, W. Huang, T. J. Marks, A. Facchetti, *J. Am. Chem. Soc.* **2020**, *142*, 5487.
[11] T. Yokota, K. Fukuda, T. Someya, *Adv. Mater.* **2021**, *33*, 2004416.
[12] J. Liu, J. Wang, Z. Zhang, F. Molina-Lopez, G.-J. N. Wang, B. C. Schroeder, X. Yan, Y. Zeng, O. Zhao, H. Tran, T. Lei, Y. Lu, Y.-X. Wang, J. B.-H. Tok, R. Dauskardt, J. W. Chung, Y. Yun, Z. Bao, *Nat. Commun.* **2020**, *11*, 3362.
[13] T. Sekitani, T. Yokota, U. Zschieschang, H. Klauk, S. Bauer, K. Takeuchi, M. Takamiya, T. Sakurai, T. Someya, *Science* **2009**, *326*, 1516.
[14] W. Jo, H. Lee, Y. Lee, B.-S. Bae, T.-S. Kim, *Adv. Eng. Mater.* **2021**, *23*, 2001280.
[15] S. Kim, H.-J. Kwon, S. Lee, H. Shim, Y. Chun, W. Choi, J. Kwack, D. Han, M. Song, S. Kim, S. Mohammadi, I. Kee, S. Y. Lee, *Adv. Mater.* **2011**, *23*, 3511.
[16] D. Yoo, D.-J. Won, W. Cho, J. Lim, J. Kim, *Adv. Mater. Technol.* **2021**, *6*, 2100358.
[17] X. Cheng, F. Zhang, R. Bo, Z. Shen, W. Pang, T. Jin, H. Song, Z. Xue, Y. Zhang, *Adv. Mater.* **2021**, *33*, 2102684.
[18] J. Royakkers, K. Guo, D. T. W. Toolan, L.-W. Feng, A. Minotto, D. G. Congrave, M. Danowska, W. Zeng, A. D. Bond, M. Al-Hashimi, T. J. Marks, A. Facchetti, F. Cacialli, H. Bronstein, *Angew. Chem., Int. Ed.* **2021**, *60*, 25005.
[19] S. T. M. Tan, G. Lee, I. Denti, G. Lecroy, K. Rozylowicz, A. Marks, S. Griggs, I. Mcculloch, A. Giovannitti, A. Salleo, *Adv. Mater.* **2022**, *34*, 2202359.
[20] B. Wang, W. Huang, S. Lee, L. Huang, Z. Wang, Y. Chen, Z. Chen, L.-W. Feng, G. Wang, T. Yokota, T. Someya, T. J. Marks, A. Facchetti, *Nat. Commun.* **2021**, *12*, 4937.
[21] Y. Yao, W. Huang, J. Chen, G. Wang, H. Chen, X. Zhuang, Y. Ying, J. Ping, T. J. Marks, A. Facchetti, *Proc. Natl. Acad. Sci. USA* **2021**, *118*, e2111790118.
[22] J. Y. Oh, S. Rondeau-Gagné, Y.-C. Chiu, A. Chortos, F. Lissel, G.-J. N. Wang, B. C. Schroeder, T. Kurosawa, J. Lopez, T. Katsumata, J. Xu, C. Zhu, X. Gu, W.-G. Bae, Y. Kim, L. Jin, J. W. Chung, J. B.-H. Tok, Z. Bao, *Nature* **2016**, *539*, 411.
[23] J. Mun, Y. Ochiai, W. Wang, Y. Zheng, Y.-Q. Zheng, H.-C. Wu, N. Matsuhisa, T. Higashihara, J. B.-H. Tok, Y. Yun, Z. Bao, *Nat. Commun.* **2021**, *12*, 3572.
[24] Z. Chen, W. Zhang, C. Wei, Y. Zhou, Y. Pan, X. Wei, J. Huang, L. Wang, G. Yu, *Chem. Mater.* **2020**, *32*, 2330.
[25] T. Higashihara, *Polym. J.* **2021**, *53*, 1061.
[26] Y. Dai, S. Dai, N. Li, Y. Li, M. Moser, J. Strzalka, A. Prominski, Y. Liu, Q. Zhang, S. Li, H. Hu, W. Liu, S. Chatterji, P. Cheng, B. Tian, I. Mcculloch, J. Xu, S. Wang, *Adv. Mater.* **2022**, *34*, 2201178.
[27] Y. Qiu, B. Zhang, J. Yang, H. Gao, S. Li, L. Wang, P. Wu, Y. Su, Y. Zhao, J. Feng, L. Jiang, Y. Wu, *Nat. Commun.* **2021**, *12*, 7038.
[28] L. Balhorn, Q. Macpherson, K. C. Bustillo, C. J. Takacs, A. J. Spakowitz, A. Salleo, *Proc. Natl. Acad. Sci. USA* **2022**, *119*, e2204346119.
[29] Y. H. Jang, Y. J. Jang, S. Kim, L. N. Quan, K. Chung, D. H. Kim, *Chem. Rev.* **2016**, *116*, 14982.
[30] K. Mishra, N. Devi, S. S. Siwal, Q. Zhang, W. F. Alsanie, F. Scarpa, V. K. Thakur, *Adv. Sci.* **2022**, *9*, 2202187.
[31] V. Vallem, Y. Sargolzaeiaval, M. Ozturk, Y.-C. Lai, M. D. Dickey, *Adv. Mater.* **2021**, *33*, 2004832.
[32] Z. Liu, Z. Yin, J. Wang, Q. Zheng, *Adv. Funct. Mater.* **2019**, *29*, 1806092.
[33] K. Pak, J. Choi, C. Lee, S. G. Im, *Adv. Electron. Mater.* **2019**, *5*, 1800799.
[34] G.-J. N. Wang, A. Gasperini, Z. Bao, *Adv. Electron. Mater.* **2018**, *4*, 1700429.
[35] T. Erdmann, S. Fabiano, B. Milián-Medina, D. Hanifi, Z. Chen, M. Berggren, J. Gierschner, A. Salleo, A. Kiriy, B. Voit, A. Facchetti, *Adv. Mater.* **2016**, *28*, 9169.
[36] L. A. Galuska, W. W. Mcnutt, Z. Qian, S. Zhang, D. W. Weller, S. Dhakal, E. R. King, S. E. Morgan, J. D. Azoulay, J. Mei, X. Gu, *Macromolecules* **2020**, *53*, 6032.

[37] X. Zhao, Y. Zhao, Q. Ge, K. Butrouna, Y. Diao, K. R. Graham, J. Mei, *Macromolecules* **2016**, *49*, 2601.
[38] E. L. Melenbrink, K. M. Hilby, M. A. Alkhadra, S. Samal, D. J. Lipomi, B. C. Thompson, *ACS Appl. Mater. Interface* **2018**, *10*, 38.
[39] S. Ghosh, N. Rolland, I. Zozoulenko, *Appl. Phys. Lett.* **2021**, *118*, 223302.
[40] A. F. Paterson, S. Singh, K. J. Fallon, T. Hodsden, Y. Han, B. C. Schroeder, H. Bronstein, M. Heeney, I. Mcculloch, T. D. Anthopoulos, *Adv. Mater.* **2018**, *30*, 1801079.
[41] C. Lee, G. Kim, Y. Chou, B. L. Musicó, M. C. Gao, K. An, G. Song, Y.-C. Chou, V. Keppens, W. Chen, P. K. Liaw, *Sci. Adv.* **2020**, *6*, eaaz4748.
[42] Z. Zeng, F. Jiang, Y. Yue, D. Han, L. Lin, S. Zhao, Y.-B. Zhao, Z. Pan, C. Li, G. Nyström, J. Wang, *Adv. Mater.* **2020**, *32*, 1908496.
[43] M. Ha, S. Lim, S. Cho, Y. Lee, S. Na, C. Baig, H. Ko, *ACS Nano* **2018**, *12*, 3964.
[44] P. J. Flory, M. Volkenstein, *Biopolymers* **1969**, *8*, 699.
[45] J. M. Torres, C. Wang, E. B. Coughlin, J. P. Bishop, R. A. Register, R. A. Riggleman, C. M. Stafford, B. D. Vogt, *Macromolecules* **2011**, *44*, 9040.
[46] M. Xiao, B. Kang, S. B. Lee, L. M. A. Perdigão, A. Luci, D. A. Warr, S. P. Senanayak, M. Nikolka, M. Statz, Y. Wu, A. Sadhanala, S. Schott, R. Carey, Q. Wang, M. Lee, C. Kim, A. Onwubiko, C. Jellett, H. Liao, W. Yue, K. Cho, G. Costantini, I. Mcculloch, H. Sirringhaus, *Adv. Mater.* **2020**, *32*, 2000063.
[47] C. Li, A. Iscen, H. Sai, K. Sato, N. A. Sather, S. M. Chin, Z. Álvarez, L. C. Palmer, G. C. Schatz, S. I. Stupp, *Nat. Mater.* **2020**, *19*, 900.
[48] J. F. Franco-Gonzalez, N. Rolland, I. V. Zozoulenko, *ACS Appl. Mater. Interfaces* **2018**, *10*, 29115.
[49] J. Choi, W. Kim, D. Kim, S. Kim, J. Chae, S. Q. Choi, F. S. Kim, T.-S. Kim, B. J. Kim, *Chem. Mater.* **2019**, *31*, 3163.
[50] S. G. Bucella, A. Luzio, E. Gann, L. Thomsen, C. R. Mcneill, G. Pace, A. Perinot, Z. Chen, A. Facchetti, M. Caironi, *Nat. Commun.* **2015**, *6*, 8394.
[51] H. Shim, F. Ershad, S. Patel, Y. Zhang, B. Wang, Z. Chen, T. J. Marks, A. Facchetti, C. Yu, *Nat. Electron.* **2022**, *5*, 660.
[52] H. Shim, K. Sim, B. Wang, Y. Zhang, S. Patel, S. Jang, T. J. Marks, A. Facchetti, C. Yu, *Nat. Electron.* **2023**, *6*, 349.
[53] D. Zhao, D. Gao, X. Wu, B. Li, S. Zhang, Z. Li, Q. Wang, Z. Wu, C. Zhang, W. C. H. Choy, X. Zhong, Q. He, Z. Zhu, *Adv. Mater.* **2022**, *34*, 2204661.
[54] A. I. Jewett, D. Stelter, J. Lambert, S. M. Saladi, O. M. Roscioni, M. Ricci, L. Autin, M. Maritan, S. M. Bashusqeh, T. Keyes, R. T. Dame, J.-E. Shea, G. J. Jensen, D. S. Goodsell, *J. Mol. Biol.* **2021**, *433*, 166841.
[55] S. Plimpton, *J. Comput. Phys.* **1995**, *117*, 1.
[56] R. W. Hockney, J. W. Eastwood, *Computer Simulation Using Particles*, CRC Press, Boca Raton, **1988**.
[57] J. F. Franco-Gonzalez, I. V. Zozoulenko, *J. Phys. Chem. B* **2017**, *121*, 4299.